Phase and microstructural characterizations for $Ce_{0.8}Gd_{0.2}O_{2-\delta}$-$FeCo_2O_4$ dual phase oxygen transport membranes

Fanlin Zeng[1,2,*], Jürgen Malzbender[1], Stefan Baumann[1], Manja Krüger[1], Louis Winnubst[2], Olivier Guillon[1], Wilhelm A. Meulenberg[1,2]

[1]Forschungszentrum Jülich GmbH, Institute of Energy and Climate Research (IEK), 52425 Jülich, Germany
[2]Inorganic Membranes, MESA+ Institute for Nanotechnology, University of Twente, P.O. Box 217, 7500 AE Enschede, The Netherlands

Abstract

Dual phase oxygen transport membranes were prepared via solid state reaction at 1200 °C. The phase compositions and microstructures of the membranes were characterized via X-ray diffraction, scanning electron microscopy and electron backscatter diffraction, and associated with image analysis and calculations to quantify microstructural features including volume fractions, grain sizes, and contiguity. The characterizations reveal a multi-phase system containing $Ce_{1-x}Gd_xO_{2-\delta'}$ ($x \approx 0.1$) (CGO10), and $Fe_yCo_{3-y}O_4$ ($0.2 < y < 1.2$) (FCO), CoO and $Gd_{0.85}Ce_{0.15}Fe_{0.75}Co_{0.25}O_3$ (GCFCO) in the sintered membranes. In addition, a novel model is utilized to assess the evolution of the ambipolar conductivity with respect to microstructural features. Both experimental and calculated results indicate that if the grain sizes of all phases in the composites are similar, the optimal ambipolar conductivity is reached with a volume ratio of ionic conducting phase to electronic conducting phase close to 4:1. Meanwhile, the GCFCO phase dominates the effective electronic conductivity.

Keywords: dual phase oxygen transport membrane, ceramic, conductivity, microstructure, optimization

1. Introduction

Mixed ionic-electronic conducting (MIEC) membranes provide, due to their almost 100% selectivity with respect to oxygen, high efficiency in terms of pure oxygen separation [1], oxyfuel coal combustion [2] and petro-chemical processes [3]. Typical perovskite-type single phase MIEC membranes, such as $Ba_{0.5}Sr_{0.5}Co_{0.8}Fe_{0.2}O_{3-\delta}$ [4] and $La_{0.6}Sr_{0.4}Co_{0.2}Fe_{0.8}O_{3-\delta}$ [5], achieve high oxygen fluxes but suffer from carbonation or sulfating reaction induced phase instabilities at elevated temperature on exposure to CO_2 or SO_2 [6, 7].

Dual phase oxygen transport membranes become recently the focus of scientific studies. They consist of separate ionic and electronic conducting phases, and exhibit good chemical stability under flue gas conditions [8]. Their oxygen permeability can be optimized by either selecting high performance and stable individual conducting phases, and/or tailoring microstructural factors like phase volume fraction, grain size, and spatial distribution of the phases [9-11]. The selection of conducting materials permits flexibility since plenty of ionic and electronic conducting phases have been developed and tested regarding their individual performance [12-15].

*Corresponding author
Email: f.zeng@fz-juelich.de
Tel.: ++49-2461-619399
Fax: ++49-2461-612455

However, microstructural aspects are more challenging since their influence on properties are not fully understood. For example, it has been suggested that a minor phase should possess a volume fraction above 30% to form percolation to obtain high ambipolar conductivity and permeability [1]. Besides, the grain size of the minor phase was recommended to be smaller or equal to that of the matrix phase [9, 11, 16]. However, for composites with a minor phase volume of less than 30%, good oxygen permeability was also reported, such as for 80 vol% $Ce_{0.8}Sm_{0.2}O_{2-\delta}$: 20 vol.% $PrBaCo_2O_{5+\delta}$ with a fiber-shaped electronic conductive skeleton [17], and for 81.5 vol% $Ce_{0.8}Gd_{0.2}O_{2-\delta}$: 18.5 vol% $FeCo_2O_4$ with a multi-phase system consisting of the $Ce_{1-x}Gd_xO_{2-\delta'}$ ($0< x <0.2$) (CGO) fluorite phase, the $Fe_yCo_{3-y}O_4$ ($0 < y < 2$) (FCO) spinel phase, the (Fe,Co)O rock salt phase, and the $Gd_{0.85}Ce_{0.15}Fe_{0.75}Co_{0.25}O_3$ (GCFCO) perovskite phase [8].

Based on the realization of the complex but important microstructures of dual phase oxygen transport membranes, the microstructural characterization, quantification, and optimization are essential as the initial step, especially for dual phase oxygen transport membranes that involve phase interactions. Hence, the current work reports on a detailed characterization and quantification regarding phase constituents and microstructural features for $Ce_{0.8}Gd_{0.2}O_{2-\delta}$-$FeCo_2O_4$ composites. All aspects including phase constituents, phase volume fraction, grain size, and phase contiguity are discussed, as well as the relation between these microstructure features and chemical properties.

2. Experimental

Powder mixtures of $Ce_{0.8}Gd_{0.2}O_{2-\delta}$ (CGO20) (Treibacher Industrie AG, 99%), Co_3O_4 (Merck, 99%) and Fe_2O_3 (Merck, 99%) (the mole ratio of Co_3O_4/ Fe_2O_3 was fixed at 4:3 to form $FeCo_2O_4$ (FC2O) spinel) were inserted into a polyethylene bottle with ethanol and 5 mm diameter zirconia balls, and ball milled on a roller bench for 3 days. The mass ratio of powder-ball-ethanol was set to be 1:2:3. After milling, the powders were dried at 75 ℃ for 3 days, then they were uniaxially pressed into disc shapes with a pressure of 20 MPa and sintered at 1200 ℃ for 10 h in air to obtain dense composites [18]. The obtained composites were abbreviated as CF. Finally, five CF composites, abbreviated as 50CF, 60CF, 70CFC, 85CF and 90CF, were synthesized via powder mixtures with weight fractions of CGO20 equal to 50 wt%, 60 wt%, 70 wt%, 85 wt% and 90 wt%, respectively. It should be noted, that the phase amounts and chemical composition in the sintered membrane might be different from the nominal ones in the starting powder mixtures due to phase interactions.

Crystal structures were determined via X-ray diffraction (XRD) (Empyrean, Malvern Panalytical Ltd) equipped with a Cu LFF tube, BBHD mirror, PIXcel3D detector. Crystal structure analysis and associated phase quantifications were carried out by Rietveld refinement using the software TOPAS 6 (Bruker AXS GmbH) with crystal structure data from the Inorganic Crystal Structure Database (ICSD) (FIZ Karlsruhe GmbH) as references. Microstructures were characterized via backscattered electron images and color-coded phase maps captured from data obtained by scanning electron microscope (SEM) (Merlin, Carl Zeiss Microscopy Ltd) and electron backscatter diffraction (EBSD) (NordlysNano, Oxford Instruments Ltd), respectively. Accordingly, microstructure aspects including grain size, and volume fraction of the different phases, were deduced via image analysis by the HKL Channel 5 software packages. The

porosity of the sintered membrane was deduced from the area fraction of pores based on analysis of at least three SEM pictures via ImageJ software.

The ambipolar conductivity (σ_a) is defined as a function of partial conductivity of the ionic and electronic conducting phases within the membrane composites [19, 20]:

$$\sigma_a = \frac{\sigma_{p,i} \cdot \sigma_{p,e}}{\sigma_{p,i} + \sigma_{p,e}} \quad (1)$$

where $\sigma_{p,i}$ and $\sigma_{p,e}$ represent the partial ionic and electronic conductivity, respectively.

The sum of $\sigma_{p,i}$ and $\sigma_{p,e}$ equals to the total conductivity (σ_t) [19]:

$$\sigma_t = \sigma_{p,i} + \sigma_{p,e} \quad (2)$$

The ionic transport number (t_i) and electronic transport number (t_e) are defined by equation (3) and (4), respectively [19-22]:

$$t_i = \frac{\sigma_{p,i}}{\sigma_t} \quad (3)$$

$$t_e = \frac{\sigma_{p,e}}{\sigma_t} \quad (4)$$

The sum of t_i and t_e always equals to unity to maintain electroneutrality [23].

A novel model is proposed here to estimate the effect of microstructural characteristics (e.g., volume fraction and grain size) on ambipolar conductivity. The microstructure of a randomly distributed dual phase oxygen transport composite can be disassembled into an equivalent structure containing three portions: effective ionic conducting portion (I), effective electronic conducting portion (II) and insulated portion (III), as presented by schematic diagrams in Figure 1. The effective ionic/electronic conducting portion is a continuous medium (see Figure 1(b)), and assumed to provide the effective ionic/electronic transport paths, and the insulated portion is not contributive to the conductivity. The volume fraction of the effective ionic/electronic conducting portion is then defined as effective volume fraction of ionic/electronic conducting phases. If ionic/electronic conducting phases in the composites possess pure ionic/electronic conductivity, and there are no frictional interactions during ionic and electronic diffusion, the partial conductivity at an equilibrium state under a given temperature and oxygen partial pressure gradient is predicted to be proportional to the effective volume fraction. And the proportionality factor is approximated as intrinsic ionic/electronic conductivity of the ionic/electronic conducting phase in a form of a dense single-phase material, as presented by equation (5) and (6):

$$\sigma_{p,i} = \sigma_i \cdot V_{eff,i} \quad (5)$$

$$\sigma_{p,e} = \sigma_e \cdot V_{eff,e} \quad (6)$$

where σ_i and σ_e are the intrinsic ionic conductivity of the ionic conducting phase and the intrinsic electronic conductivity of the electronic conducting phase, respectively. And $V_{eff,i}$ and $V_{eff,e}$ are

effective volume fractions of the ionic and electronic conducting phases within the composite, respectively. As can be seen in Figure 1(b), the volume of each conducting phase disassembled into continuous and insulated portions, hence, the cumulated effective volume fraction of ionic/electronic conducting phase is practically always less than the total volume fraction of ionic/electronic conducting phase.

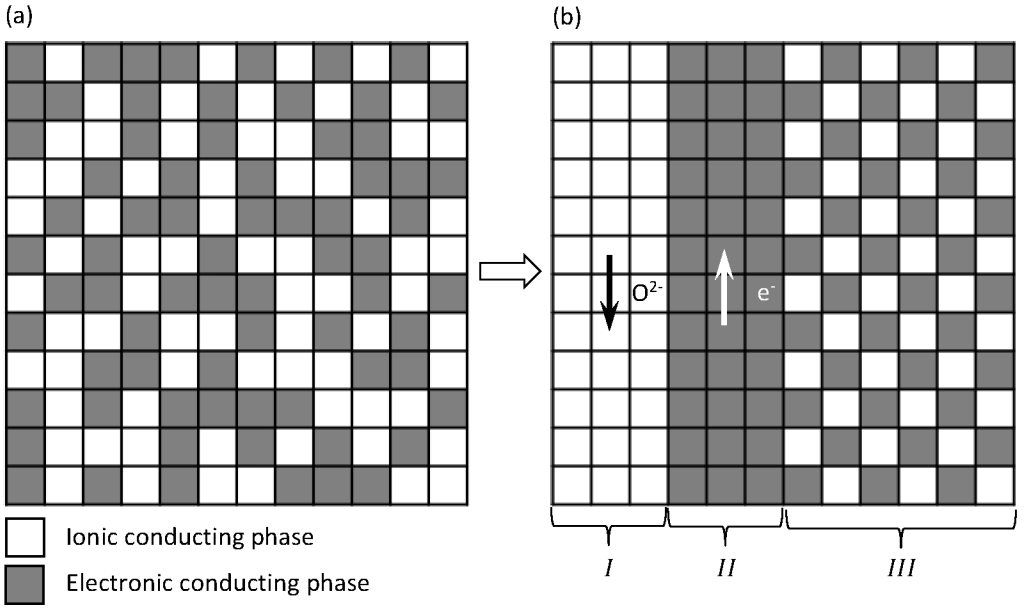

Figure 1 Schematic diagrams represent (a) microstructure of a randomly distributed dual phase oxygen transport membrane, and (b) equivalently disassembled structure of (a) [24]. (I, II and III are effective ionic conducting portion, effective electronic conducting portion and insulated portion assuming that transport can only take place across edges and not across corners, respectively)

The effective volume fraction defined here is equivalent to the parameter reported as continuous volume fraction [24], and it was also reported that continuous volume fraction of one phase within a dual phase material is equal to the product of the contiguity and the total volume fraction of this phase [25]. Hence, the effective volume fractions of ionic and electronic conducting phases are calculated by equation (7) and (8), respectively:

$$V_{eff,i} = C_i \cdot V_i \tag{7}$$

$$V_{eff,e} = C_e \cdot V_e \tag{8}$$

where V_i and V_e are the total volume fractions of ionic and electronic phases, respectively, and C_i and C_e denote the contiguities of the ionic and electronic phases, respectively.

The contiguity of a phase within a dual phase material is expressed as the fraction of the total interconnected surface area of this phase shared with particles of the same phase [26], and it is

correlated with the total volume fraction and the grain size ratio of both phases within the dual phase material, as indicated by the following equations [24, 26]:

$$C_i = \frac{V_i \cdot R}{V_i \cdot R + V_e} \tag{9}$$

$$C_e = 1 - C_i \tag{10}$$

$$R = \frac{d_e}{d_i} \tag{11}$$

where C, V, d, and R are contiguity, volume fraction, grain size and grain size ratio of electronic phase to ionic phase, respectively, and subscript i and e represent ionic and electronic phase, respectively.

Combining relations from equation (5)-(11), equation (1) can be expressed as:

$$\sigma_a = \frac{V_i^2 \cdot R \cdot \sigma_i \cdot (1 - V_i)^2 \cdot \sigma_e}{V_i^2 \cdot R \cdot \sigma_i + (1 - V_i)^2 \cdot \sigma_e} \cdot \frac{1}{1 + (R - 1) \cdot V_i} \tag{12}$$

Equation (12) provides estimations of effects of microstructural and intrinsic properties on ambipolar conductivity. In case the grain size ratio of electronic phase to ionic phase R equals 1, equation (12) simplifies to:

$$\sigma_a = \frac{V_i^2 \cdot \sigma_i \cdot (1 - V_i)^2 \cdot \sigma_e}{V_i^2 \cdot \sigma_i + (1 - V_i)^2 \cdot \sigma_e} \tag{13}$$

With known σ_i and σ_e, the influence of the volume ratio on ambipolar conductivity can be assessed by equation (13) for dual phase composite membranes.

3. Results and discussion

3.1 Microstructure characterization

The microstructures of CF composites were investigated via BSEM and EBSD. An example for 50CF is presented in Figure 2, which demonstrates the coexisting of CGO fluorite, FCO spinel, $GdFeO_3$-type perovskite, and CoO rock salt phase. The formula of $GdFeO_3$-type perovskite has been reported to be $Gd_{0.85}Ce_{0.15}Fe_{0.75}Co_{0.25}O_3$ (GCFCO) [8, 27]. FCO possesses a rather uneven grain size, being coarsely distributed among CGO. Each sample has a density that exceeds 99% (Table S1).

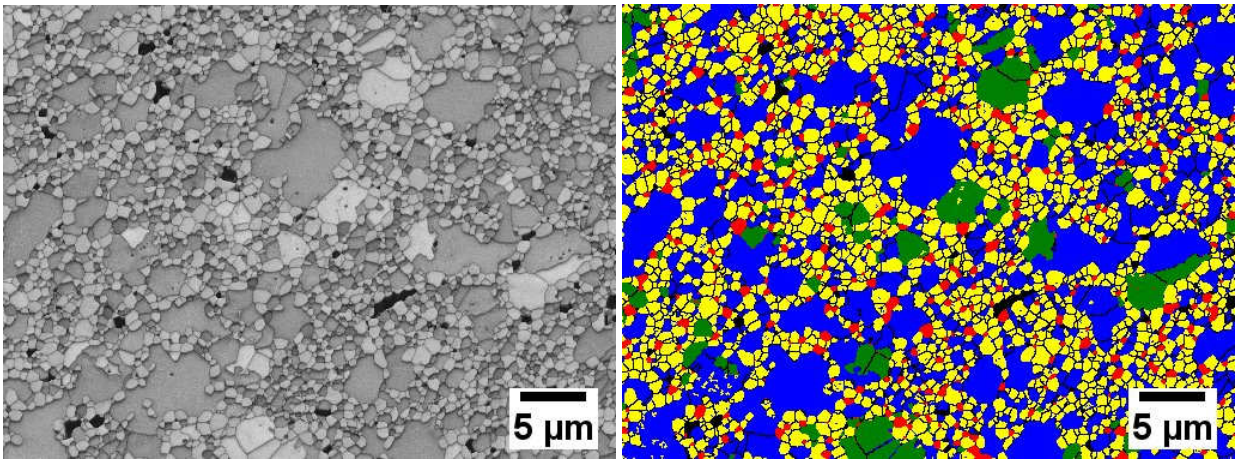

Figure 2 Microstructure investigation via BSEM (left) and EBSD phase mapping (right) on 50CF. (the yellow, red, blue and green phase are CGO, GCFCO, FCO, and CoO, respectively)

Volume fractions of each phase were obtained from EBSD phase mapping results, which can be seen in Table 1. As expected, volume fraction of CGO in the sintered composites increases with the increasing weight ratio of CGO20 to FC2O in the starting powder mixture. A relatively considerable amount of GCFCO perovskite is characterized, and the maximum GCFCO perovskite content exists for 85CF. All composites except 90CF possess a high-temperature stable CoO phase, which remains at room temperature as a result of uncompleted re-oxidization of FCO. In addition, normalized volume fractions of ionic and electronic conducting phases are also calculated, regarding CGO as ionic conducting phase and FCO, CoO and GCFCO phase as electronic conducting phases, since FCO, CoO and GCFCO phase are electronic conductive phases with negligible ionic conductivity [28].

Table 1 Volume fractions of the different phases in the CF composites sintered at 1200 °C.

Composite	CGO as ionic conducting phase (vol%)	Electronic conducting phase			
		FCO (vol%)	GCFCO (vol%)	CoO (vol%)	Sum (vol%)
50CF	40.4	43.0	5.4	11.2	59.6
60CF	52.3	32.2	7.3	8.2	47.7
70CF	66.2	21.0	8.3	4.5	33.8
85CF	80.1	9.0	10.0	0.9	19.9
90CF	93.7	3.4	3.0	0	6.4

Grain sizes were also deduced from the EBSD measurements and respective results are presented in Supplementary Table 2. The grain sizes of CGO and GCFCO are ~0.6 µm and ~0.5 µm, respectively. They

are almost the same and rather similar among all composites, while grain sizes of the FCO and CoO phases decrease slightly with increasing CGO content and possess large standard deviations.

Since the limited number of characterized FCO and CoO grains might induce large inaccuracy in the grain size calculations (Table S2), an image analysis based method was conducted via ImageJ software for comparison, but average grain sizes of FCO and CoO grains merged into one value in the calculation as FCO and CoO can hardly be separated via thresholding in backscattered electron images. Based on the rather good detection of a large number of black FCO and CoO grains (see Figure S1), the obtained average grain sizes of FCO and CoO, as shown in Table 2, are slightly larger than the ones measured via EBSD, meanwhile, they show a bimodal distribution profile with a second peak at a large grain size of ~3 µm (Figure S2), which leads to large uncertainties in the determination of the average grain sizes. The calculated average *R* values of the CF composites, as given in Table 3, vary between 1 and 2 with rather large deviations (~90%).

Table 2 Average grain size of FCO and CoO as obtained via an image analysis method.

Parameters / Composites	Number of grains	Average grain size (µm)
50CF	2525	1.2 ± 0.9
60CF	2539	1.0 ± 0.8
70CF	2276	0.9 ± 0.6
85CF	1106	0.8 ± 0.6
90CF	709	0.8 ± 0.6

Table 3 Calculated average *R* values for the CF composites.

Composite	Average *R*
50CF	1.7 ± 1.5
60CF	1.3 ± 1.2
70CF	1.3 ± 1.1
85CF	1.2 ± 1.0
90CF	1.1 ± 1.0

According to the characterized volume fractions and average grain sizes, contiguities of ionic and electronic conducting phases were calculated using equations (9)-(11). The contiguity of electronic conducting phases is lower than that of ionic conducting phase, and monotonously decreases with increasing volume fraction of ionic conducting phase, as shown in Figure 3, but the reduced *R* contributes slightly to an improvement of the contiguity of the electronic conducting phases. For a phase within a dual phase composite, higher contiguity and higher volume fraction indicates a larger continuous volume and less tendency of insulation (as can be seen by equation (7) and (8)), and hence a better percolation and will further improve the conductivity.

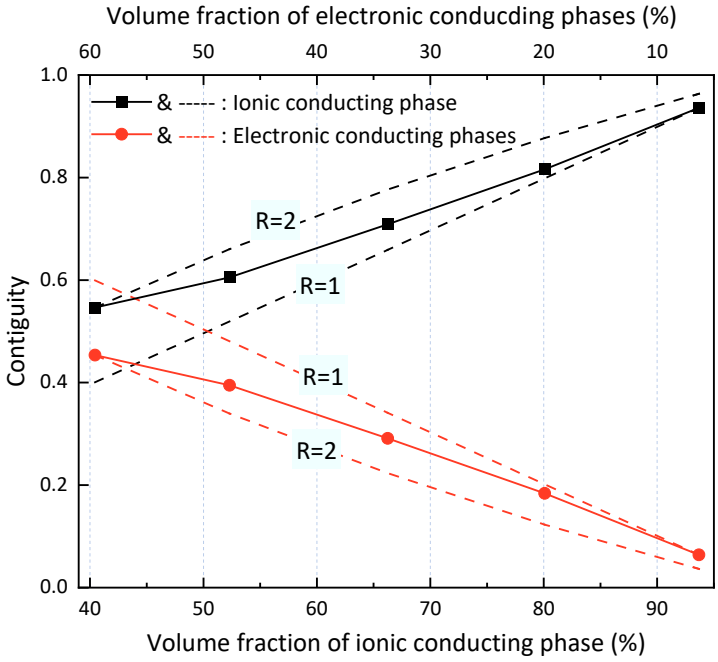

Figure 3 Contiguity of ionic and electronic conducting phases in the CF composites with solid lines as actual value and dotted lines corresponding to simulated value with associated *R* shown for each line.

3.2 Phase characterization

The phase constituents of CF composites were investigated via XRD. The XRD patterns (Figure S1) reveal a multi-phase system that is similar to the one investigated by EBSD (see Figure 2). For 50CF, 60CF and 70CF, four phases are identified: Gd-doped ceria fluorite (CGO), cobalt iron spinel (FCO) phases, GCFCO perovskite and CoO rock salt phase. But for 85CF, CoO can be hardly found and quantified by XRD due to its limited amount as revealed in Table 1. And for 90CF, it seems that diffraction patterns of CoO instead of FCO can be fitted. However, according to the volume fractions obtained from EBSD investigations (see Table 1), CoO does not appear in 90CF. Hence, diffraction patterns of FCO are fitted for 90CF to derive weight fractions. It is not possible to match any kind of cobalt iron spinel in the ICSD, which confirms coexistence of FCO spinels with variations of the cobalt to iron ratio. The lattice parameters of CGO and

GCFCO are almost identical among the composites (Table S3), which indicates a similar composition in the respective phase in each composite.

The weight fraction of each phase was deduced from the XRD data as shown in Table 4. The characterized CGO content in each sintered composite is lower than the nominal CGO20 content in the respective starting powder mixture due to phase interactions between CGO20 and FC2O. The tendency regarding the weight fraction of each phase as a function of nominal CGO20 content in the starting powder is identical in terms of the volume fraction as shown in Table 1.

Table 4 Weight fractions of the different phases in the CF composites sintered at 1200 °C.

Composite	Nominal composition		Composition after sintering at 1200 °C			
	CGO20 (wt%)	FC2O (wt%)	CGO (wt%)	FCO (wt%)	GCFCO (wt%)	CoO (wt%)
50CF	50	50	40.2	41.9	8.5	9.4
60CF	60	40	47.7	34.8	10.7	6.8
70CF	70	30	59.0	25.2	10.9	4.9
85CF	85	15	70.9	14.5	14.6	0
90CF	90	10	83.5	4.2	12.3	0

The formation of the GCFCO perovskite consumes Gd from CGO20 as well as Fe and Co from FC2O. The phase reaction is presented in equation (14).

Since the ionic conductivity of Gd-doped cerium oxide depends on the Gd content [29, 30] and the electronic conductivity of cobalt iron oxide is a result of the ratio of Fe to Co [31], it is necessary to determine the stoichiometry of Gd, i.e, x, in the Gd-doped cerium oxide and the one of Fe, i.e., y, in the cobalt iron spinel formed in the prepared composites. Hence, x and y were calculated by equation (15)&(16) and (17)&(18), respectively. The parameters a and b were known inputs, and the f and g were deduced from the characterized weight fraction from the XRD patterns (Table 4).

$$a\ Ce_{0.8}Gd_{0.2}O_{2-\delta} + b\ Co_3O_4 + 0.75 \cdot b\ Fe_2O_3 + c\ O_2 = d\ Ce_{1-x}Gd_xO_{2-\delta'} + e\ Fe_yCo_{3-y}O_4 + f\ Gd_{0.85}Ce_{0.15}Fe_{0.75}Co_{0.25}O_3 + g\ CoO + h\ O_2 \quad (14)$$

$$0.8 \cdot a = (1-x) \cdot d + 0.15 \cdot f \quad (15)$$

$$0.2 \cdot a = d \cdot x + 0.85 \cdot f \quad (16)$$

$$3 \cdot b = e \cdot (3-y) + 0.25 \cdot f + g \quad (17)$$

$$1.5 \cdot b = e \cdot y + 0.75 \cdot f \quad (18)$$

where a, b, d, e, f, g are stoichiometric coefficients of $Ce_{0.8}Gd_{0.2}O_{2-\delta}$ (CGO20), Co_3O_4, Fe_2O_3, $Ce_{1-x}Gd_xO_{2-\delta'}$ (CGO), $Fe_yCo_{3-y}O_4$ (FCO), $Gd_{0.85}Ce_{0.15}Fe_{0.75}Co_{0.25}O_3$ (GCFCO) and CoO phases, respectively. The parameters c and h are stoichiometric coefficients of O_2. The subscripts δ and δ' refer to the oxygen non-stoichiometry.

The calculated results are presented in Table 5. The average CGO in the CF composites can be characterized as $Ce_{0.9}Gd_{0.1}O_{2-\delta'}$ (CGO10) since the average stoichiometry of Gd in CGO is close to 0.1 and almost independent of CGO content in the CF composites. The stoichiometry of Fe in FCO, however, varies between ~0.2-1.2. It should be noted, that there is a small amount of CoO in 85CF, which is not capable to be quantified by XRD, but it induces limited errors in derived y value of 85CF. Thus, it can be concluded that the formation of the GCFCO phase consumes maximally about 50% of the Gd in CGO20 with sufficient stoichiometry of Fe. But it should be pointed out that among different grains the stoichiometry might locally deviate from the average value.

Table 5 Calculated average *x* in $Ce_{1-x}Gd_xO_{2-\delta'}$ (CGO) and *y* in $Fe_yCo_{3-y}O_4$ (FCO).

Composite	*x*	*y*
50CF	0.12	1.18
60CF	0.11	1.10
70CF	0.12	1.04
85CF	0.12	0.47
90CF	0.13	0.24

3.3 Effect of microstructure parameters on ambipolar conductivity

The oxygen permeation through the membrane is controlled by both oxygen surface exchange and ambipolar bulk diffusion of oxygen ions and electrons [1]. When the surface exchange is rather fast compared to the bulk diffusion, the ambipolar conductivity is dominating [1], and this ambipolar conductivity can then be predicted by equations (12) or (13) with consideration of the influence from microstructure aspects, such as volume fraction, grain size and contiguity.

Since the studied composites contained two main electronic conducting phases, i.e. GCFCO and $Fe_yCo_{3-y}O_4$ ($0.2 < y < 1.2$), but only one ionic conducting phase, i.e., CGO (can be estimated as CGO10), calculations of the ambipolar conductivity via equation (13) were performed for three assumed dual phase composites with an R value equals to 1. One of the assumed composites consists of CGO10 and GCFCO, abbreviated as CGO10&GCFCO, the other one contains CGO10 and $FeCo_2O_4$, named as CGO10&FC2O, and the last one composes of CGO10 and Co_3O_4, denoted as CGO10&Co_3O_4. The

ambipolar conductivities of the CF composites are expected to be higher than that of CGO10&GCFCO but lower than that of CGO10&FC2O and CGO10&Co_3O_4. CoO is not considered here because CoO is only stable at a temperature above 950 ℃ [32], below which CoO tends to be gradually oxidized into spinel with time.

The O_2 permeation conditions for the calculation of ambipolar conductivity was set to be at a temperature of 800 ℃, and the atmospheres of two sides of the membrane were selected to be air and Ar, respectively. Necessary inputs for equation (13) include the volume fraction of ionic/electronic conducting phase and the conductivity of each phase under the selected calculation conditions. Although FCO segregation and reduction were investigated at the surfaces of the CF materials in the temperature range of ~700-1000 ℃ with an air/Ar gradient, phase structures and compositions in the bulk are rather stable [8]. Hence, the volume fractions of ionic/electronic conducting phases under the selected O_2 permeation conditions are considered as approximately the same as the investigated ones at room temperature. Meanwhile, the electronic conductivity of GCFCO and FCO for the calculation of ambipolar conductivity is estimated to be the same as the one in air at 800 ℃, as listed in Table 6. Since the stoichiometry of Fe in FCO varies between 0.2 and 1.2 (see Table 5), the upper and lower bound for electronic conductivity of FCO are assumed to be equal to the electronic conductivity of Co_3O_4 and FC2O, respectively. Besides, although CGO10 exhibits electronic conductivity in addition to ionic conductivity under low oxygen partial pressure [33], it was reported for CGO10 that in Ar atmosphere (~10^{-5} atm) and at a temperature of 800 ℃, the total conductivity is almost equal to the ionic conductivity [29]. In the O_2 permeation test, Ar is used as a sweep gas, which is continuously enriched in oxygen and, thus, the low oxygen partial pressure is fairly above 10^{-5} atm, which indicates that the experimental conditions can hardly be sufficient to reduce Ce^{4+} to Ce^{3+} and, hence does not significantly induce small polarons in CGO10. Therefore, for the calculation of ambipolar conductivity, CGO10 is regarded as a pure ionic conducting phase with an ionic conductivity estimated to be the same as the one measured in air at 800 ℃ as shown in Table 6.

Accordingly, the ambipolar conductivity was calculated as a function of volume fraction of ionic/electronic conducting phase as presented in Figure 4. Meanwhile, the experimental ambipolar conductivities of 60CF, 85CF, and 90CF were also shown in Figure 4. These experimental values were deduced via equation (19) based on oxygen permeation results at 800 ℃ that have been reported for the CF composites with a verified *R* value close to 1 [8, 28, 34]:

$$\sigma_a = \frac{16 \cdot L \cdot F^2 \cdot j_{O_2}}{R \cdot T} / \ln \frac{p_{O_2}^{feep}}{p_{O_2}^{sweed}} \tag{19}$$

where j_{O_2} is the oxygen flux, *L* the thickness of the membrane, *T* the temperature, *R* the gas constant, *F* the Faraday constant, and the $p_{O_2}^{feed}$ and $p_{O_2}^{sweep}$ are the oxygen partial pressures at the feed and sweep side, respectively.

Table 6 Ionic and electronic conductivity of the different phases at 800 ℃ in air.

Phase		Conductivity (S/cm)		Reference
		σ_i	σ_e	
$Ce_{0.9}Gd_{0.1}O_{2-\delta'}$		0.075	-	[29, 30]
$Gd_{0.85}Ce_{0.15}Fe_{0.75}Co_{0.25}O_3$		-	2.56	[8]
$Fe_yCo_{3-y}O_4$ $(0.2 < y < 1.2)$	lower bound: Co_3O_4	-	6.7	[35, 36]
	upper bound: $FeCo_2O_4$	-	19.8	[8]

The calculated curves (see Figure 4) indicate that the maximum σ_a improves when CGO10 partners with an electronic conducting phase with higher electronic conductivity, meanwhile more CGO10 content is necessary to achieve the maximum σ_a. The maximum σ_a for CGO10&GCFCO, CGO10&Co_3O_4, and CGO10&FC2O appears when CGO10 is ~76 vol%, ~82 vol%, and ~87 vol%, respectively. The composite with ~87 vol% CGO10 and ~13 vol% FC2O possesses the highest σ_a among the ones calculated for all composites.

In contrast to calculation results, the experimental σ_a of the CF composites, except 60CF, are located between the calculated σ_a of CGO10&GCFCO and CGO10&FC2O. The experimental σ_a of 90CF is located slightly above the calculated σ_a of CGO10&Co_3O_4, it could be owing to the fact that the FCO spinel in 90CF possesses a small amount of Fe (see Table 5), and exhibits a higher electronic conductivity than that of Co_3O_4 [31]. Furthermore, the highest experimental σ_a of the CF composites is lower than the calculated ones of CGO10&Co_3O_4 and CGO10&FC2O, but rather close to the one of CGO10&GCFCO. This infers that GCFCO is dominating the effective electronic conductivity in the CF composites with the highest σ_a, i.e. 85CF, among all the electronic conducting phases. However, according to the study on 60 vol% $Ce_{0.8}Gd_{0.2}O_{2-\delta}$: 40 vol% Fe_2CoO_4 composite [37], the newly formed perovskites are completely isolated. With similar phase constituents, 85CF is expected to form also a poorly connected GCFCO. Therefore, the effective electronic conductivity of 85CF relies on the electronic conductive network formed by GCFCO and FCO, and is determined by the component with the lowest electronic conductivity, i.e. GCFCO [28].

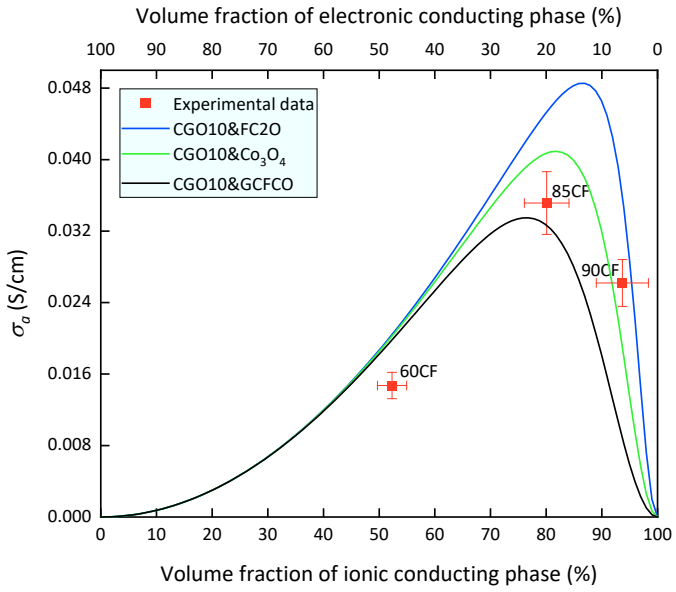

Figure 4 Ambipolar conductivity as a function of volume fraction of ionic/electronic conducting phase when *R* = 1.

For 85CF with an *R* value larger than 1 as shown in this study, the σ_a was determined to be ~0.021 S/cm at 800 ℃ as derived via equation (19) on the basis of reported oxygen permeation results [18]. It is much lower than the σ_a of 85CF with *R* being close to 1, since the larger FCO grains cannot bridge the GCFCO grains as good as the small FCO grains can do this. Therefore, future improvement of the performance will rely on the reduction of the grain size of FCO.

4. Conclusions

Phase and microstructure characterizations were carried out for CF composites prepared via solid state reaction. It reveals the formation of $Ce_{1-x}Gd_xO_{2-\delta'}$ ($x \approx 0.1$), $Fe_yCo_{3-y}O_4$ ($0.2 < y < 1.2$), CoO and a newly formed perovskite phase - $Gd_{0.85}Ce_{0.15}Fe_{0.75}Co_{0.25}O_3$. Meanwhile, the grain size ratio of electronic conducting phases (i.e., FCO, CoO and GCFCO) to ionic conducting phase (i.e., CGO10) is between 1 and 2 with a large standard deviation, since grain sizes of FCO and CoO are rather large and uneven.

New equations are proposed to assess the evolution of ambipolar conductivity as a function of the composition and grain size ratio of the two phases. When *R* is close to 1, the measured σ_a of 85CF and 90CF are located between the calculated ones of CGO10&FC2O and CGO10&GCFCO. Furthermore, the measured highest ambipolar conductivity for the CF composites is achieved for 85CF with ~80 vol% CGO10, it is much close to the calculated one for CGO10&GCFCO with ~76 vol% CGO10; Thus, the GCFCO dominates the effective electronic conductivity in the electronic conductive network formed by FCO and GCFCO in bulk of 85CF in the oxygen permeation process. Furthermore, small FCO grains contribute to bridging the GCFCO gains and improving the ambipolar conductivity.

Overall, the new material combination provides the basis of a viable high-performance oxygen-separation membrane at least for applications with oxidizing atmospheres, such as oxy-combustion processes. Although the stability of the spinel phase is rather limited in low oxygen partial pressure, e.g. membrane reactors, this phase is partly transformed into the naturally more stable perovskite during sintering. Therefore, the solid state reactive sintering approach paves the way to further material development covering a wide range of applications. Nevertheless, specific stability testing in targeted application conditions is mandatory for any kind of material because long term stability is key to success for proving novel technologies such as membrane reactors.

Acknowledgements

Financial support of this work is given by China Scholarship Council. The authors gratefully acknowledge Dr. E. Wessel, Dr. D. Grüner and Mr. M. Ziegner for their great contributions on characterization of phase structures and microstructures. Meanwhile, the authors also greatly thank the support from Prof. Dr. L. Singheiser and Prof. Dr. R. Schwaiger.

References

[1] X. Zhu, W. Yang, Mixed conducting ceramic membranes, Springer, Dalian, China, 2017.
[2] H. Stadler, F. Beggel, M. Habermehl, B. Persigehl, R. Kneer, M. Modigell, P. Jeschke, Oxyfuel coal combustion by efficient integration of oxygen transport membranes, International Journal of Greenhouse Gas Control 5(1) (2011) 7-15.
[3] Z. Cao, H. Jiang, H. Luo, S. Baumann, W.A. Meulenberg, J. Assmann, L. Mleczko, Y. Liu, J. Caro, Natural gas to fuels and chemicals: improved methane aromatization in an oxygen-permeable membrane reactor, Angewandte Chemie International Edition 52(51) (2013) 13794-13797.
[4] S. Baumann, J. Serra, M. Lobera, S. Escolástico, F. Schulze-Küppers, W. Meulenberg, Ultrahigh oxygen permeation flux through supported $Ba_{0.5}Sr_{0.5}Co_{0.8}Fe_{0.2}O_{3-\delta}$ membranes, Journal of Membrane Science 377(1-2) (2011) 198-205.
[5] J.M. Serra, J. Garcia-Fayos, S. Baumann, F. Schulze-Küppers, W. Meulenberg, Oxygen permeation through tape-cast asymmetric all-$La_{0.6}Sr_{0.4}Co_{0.2}Fe_{0.8}O_{3-\delta}$ membranes, Journal of membrane science 447 (2013) 297-305.
[6] M. Arnold, H. Wang, A. Feldhoff, Influence of CO_2 on the oxygen permeation performance and the microstructure of perovskite-type $(Ba_{0.5}Sr_{0.5})(Co_{0.8}Fe_{0.2})O_{3-\delta}$ membranes, Journal of Membrane Science 293(1-2) (2007) 44-52.
[7] A. Waindich, A. Möbius, M. Müller, Corrosion of $Ba_{1-x}Sr_xCo_{1-y}FeyO_{3-\delta}$ and $La_{0.3}Ba_{0.7}Co_{0.2}Fe_{0.8}O_{3-\delta}$ materials for oxygen separating membranes under Oxycoal conditions, Journal of Membrane Science 337(1-2) (2009) 182-187.
[8] M. Ramasamy, E. Persoon, S. Baumann, M. Schroeder, F. Schulze-Küppers, D. Görtz, R. Bhave, M. Bram, W. Meulenberg, Structural and chemical stability of high performance $Ce_{0.8}Gd_{0.2}O_{2-\delta}$-$FeCo_2O_4$ dual phase oxygen transport membranes, Journal of Membrane Science 544 (2017) 278-286.
[9] X. Zhu, H. Wang, W. Yang, Relationship between homogeneity and oxygen permeability of composite membranes, Journal of Membrane Science 309(1-2) (2008) 120-127.
[10] H. Luo, H. Jiang, K. Efimov, J. Caro, H. Wang, Influence of the preparation methods on the microstructure and oxygen permeability of a CO_2-stable dual phase membrane, AIChE Journal 57(10) (2011) 2738-2745.
[11] Q. Li, X. Zhu, Y. He, Y. Cong, W. Yang, Effects of sintering temperature on properties of dual-phase oxygen permeable membranes, Journal of membrane science 367(1-2) (2011) 134-140.
[12] B.C. Steele, Ceramic ion conducting membranes, Current Opinion in Solid State Materials Science 1(5) (1996) 684-691.
[13] V. Kharton, A. Kovalevsky, A. Viskup, A. Shaula, F. Figueiredo, E. Naumovich, F. Marques, Oxygen transport in $Ce_{0.8}Gd_{0.2}O_{2-\delta}$-based composite membranes, Solid State Ionics 160(3-4) (2003) 247-258.
[14] A. Petric, H. Ling, Electrical Conductivity and Thermal Expansion of Spinels at Elevated Temperatures, Journal of the American Ceramic Society 90(5) (2007) 1515-1520.

[15] E. Verwey, P. Haayman, F. Romeijn, Physical properties and cation arrangement of oxides with spinel structures II. Electronic conductivity, The Journal of Chemical Physics 15(4) (1947) 181-187.
[16] H. Li, X. Zhu, Y. Liu, W. Wang, W. Yang, Comparative investigation of dual-phase membranes containing cobalt and iron-based mixed conducting perovskite for oxygen permeation, Journal of membrane science 462 (2014) 170-177.
[17] T. Chen, H. Zhao, Z. Xie, J. Wang, Y. Lu, N. Xu, $Ce_{0.8}Sm_{0.2}O_{2-\delta}$-$PrBaCo_2O_{5+\delta}$ dual-phase membrane: Novel preparation and improved oxygen permeability, Journal of Power Sources 223 (2013) 289-292.
[18] M. Ramasamy, Dual phase oxygen transport membrane for efficient oxyfuel combustion, Doctoral dissertation, Bochum University, Bochum, Germany, 2016.
[19] S.G. Patrício, E.I. Papaioannou, B.M. Ray, I.S. Metcalfe, F.M.B. Marques, Composite CO_2 separation membranes: Insights on kinetics and stability, Journal of Membrane Science 541 (2017) 253-261.
[20] F.M.B. Marques, S.G. Patrício, E. Muccillo, R. Muccillo, On the model performance of composite CO_2 separation membranes, Electrochimica Acta 210 (2016) 87-95.
[21] E. Vøllestad, H. Zhu, R.J. Kee, Interpretation of defect and gas-phase fluxes through mixed-conducting ceramics using Nernst-Planck-Poisson and integral formulations, Journal of The Electrochemical Society 161(1) (2014) F114-F124.
[22] X. Tan, S. Liu, K. Li, R. Hughes, Theoretical analysis of ion permeation through mixed conducting membranes and its application to dehydrogenation reactions, Solid State Ionics 138(1-2) (2000) 149-159.
[23] K. Li, Ceramic membranes for separation and reaction, John Wiley & Sons, London, United Kingdom, 2007.
[24] Z. Fan, A. Miodownik, P. Tsakiropoulos, Microstructural characterisation of two phase materials, Materials science technology 9(12) (1993) 1094-1100.
[25] H.-C. Lee, J. Gurland, Hardness and deformation of cemented tungsten carbide, Materials science and engineering 33(1) (1978) 125-133.
[26] J. Gurland, The measurement of grain contiguity in two-phase alloys, Transactions of the Metallurgical Society of AIME 212 (1958) 452-455.
[27] F. Zeng, J. Malzbender, S. Baumann, F. Schulze-Küppers, M. Krüger, A. Nijmeijer, O. Guillon, W.A. Meulenberg, Micro-mechanical characterization of $Ce_{0.8}Gd_{0.2}O_{2-\delta}$-$FeCo_2O_4$ dual phase oxygen transport membranes, Advanced Engineering Materials (2020).
[28] M. Ramasamy, S. Baumann, A. Opitz, R. Iskandar, J. Mayer, D. Udomsilp, U. Breuer, M. Bram, Phase Interaction and Distribution in Mixed Ionic Electronic Conducting Ceria-Spinel Composites, Advances in Solid Oxide Fuel Cells Electronic Ceramics II: Ceramic Engineering Science Proceedings Volume 37, Issue 3 37 (2017) 99-112.
[29] S. Wang, T. Kobayashi, M. Dokiya, T. Hashimoto, Electrical and ionic conductivity of Gd-doped ceria, Journal of The Electrochemical Society 147(10) (2000) 3606-3609.
[30] J.H. Joo, G.S. Park, C.-Y. Yoo, J.H. Yu, Contribution of the surface exchange kinetics to the oxygen transport properties in $Gd_{0.1}Ce_{0.9}O_{2-\delta}$-$La_{0.6}Sr_{0.4}Co_{0.2}Fe_{0.8}O_{3-\delta}$ dual-phase membrane, Solid State Ionics 253 (2013) 64-69.
[31] T. Kiefer, Entwicklung neuer Schutz-und Kontaktierungsschichten für Hochtemperatur-Brennstoffzellen, Ruhr-Universität Bochum, Universitätsbibliothek (2008).
[32] P.J. Murray, J.W. Linnett, Mössbauer studies in the spinel system $Co_xFe_{3-x}O_4$, Journal of Physics and Chemistry of Solids 37(6) (1976) 619-624.
[33] S.-H. Park, H.-I. Yoo, Defect-chemical role of Mn in Gd-doped CeO_2, Solid State Ionics 176(15-16) (2005) 1485-1490.
[34] M. Ramasamy, S. Baumann, J. Palisaitis, F. Schulze-Küppers, M. Balaguer, D. Kim, W.A. Meulenberg, J. Mayer, R. Bhave, O. Guillon, Influence of Microstructure and Surface Activation of Dual-Phase Membrane $Ce_{0.8}Gd_{0.2}O_{2-\delta}$-$FeCo_2O_4$ on Oxygen Permeation, Journal of the American Ceramic Society 99(1) (2016) 349-355.
[35] E.M. Garcia, The electrochemical behavior of cobalt electrodeposits on 430 stainless steel as solid oxide fuel cell interconnect, Surface and Coatings Technology 235 (2013) 10-14.
[36] Y. Ji, J.A. Kilner, M.F. Carolan, Electrical conductivity and oxygen transfer in gadolinia-doped ceria (CGO)-$Co_3O_{4-\delta}$ composites, Journal of the European Ceramic Society 24(14) (2004) 3613-3616.
[37] W.M. Harris, K.S. Brinkman, Y. Lin, D. Su, A.P. Cocco, A. Nakajo, M.B. DeGostin, Y.-c.K. Chen-Wiegart, J. Wang, F. Chen, Characterization of 3D interconnected microstructural network in mixed ionic and electronic conducting ceramic composites, Nanoscale 6(9) (2014) 4480-4485.